Reduced order borehole induction modelling

N. Ardjmandpour[1], C. Pain[2], F. Fang[2], J. Singer[1], M. A. Player[1], Xu Xu[1], I. M. Navon[3], J. Carter[2]

[1] *GE Energy Oilfield Technology, Building X 107, Range Road, Cody Technology Park, Farnborough, Hampshire, GU14 0FG, UK*

[2] *Department of Earth Science and Engineering, Imperial College London, South Kensington Campus, Exhibition Road, London SW7 2AZ, UK*

[3] *Department of Scientific Computing, Florida State University, Tallahassee, FL 32306-4120, U.S.A.*

SUMMARY

The development of the reduced order model, Proper Orthogonal Decomposition (POD) method, for array induction tool has been demonstrated in this paper for the first time. The motivation behind the reduced order modelling is that numerical simulation of Maxwell equations is too expensive in terms of computational time for the purpose of inversion, where the forward model needs to be run many times. In this study, we demonstrate that the POD model is fast and accurate for an iterative inversion to estimate the formation conductivity. The POD method optimally extracts a few fundamental modes or basis functions from the numerical/experimental solutions, that can accurately represent the most energy in the original dynamic system. The solutions can be reconstructed as a linear combination of the POD basis functions through Galerkin projection. POD provides a low-dimensional description of the system's dynamics, which is an order of magnitude smaller than the dimension of the full forward model. The POD model is applied to the numerical solutions obtained from a finite element forward model. The results show that the POD solutions agree well with the ones obtained from the forward model.

Key words: POD, reduced order model, array induction tool, Maxwell equations.

1   Introduction

The goal of processing induction log signals is to invert measured responses and obtain the estimates of the true formation conductivity profiles. The conductivity can be used to infer the fluid content of geological formations, where lower conductivity (higher resistivity) is typically associated with those formations that bear hydrocarbons.

When inverting the measured induction log signal to estimate the formation conductivity, one uses an iterative optimization technique based on a forward model. However, the use of a

forward model based on the solution of the partial differential equation (PDE) using an approach such as Finite Element (FE) is very expensive in terms of the computer time (Lin et al., 1984). Anderson and Gianzero (1983) developed a 1D spectral integral code which computes induction response in an arbitrary number of planar layered media. Although their fast forward model can significantly improve the speed compared to the forward model with FE method (Lin et al., 1984; Dyos, 1987; Freedman and Minerbo, 1991), these models are still not fast enough for determination of inversions that could lead to well-site identification. The approximation to the forward model such as Born approximation (Thadani et al., 1983) based on geometrical factor theory (Doll, 1949; Moran, 1982), could considerably speed up the inversion process (Dyos, 1987; Freedman and Minerbo, 1991). The drawback of this approximation is that it breaks down for high conductivity beds or where there are large contrasts in the formation conductivity.

To speed up the inversion process, one can replace the forward model by a fast forward model such as a neural network, where the layer conductivities are inputs and the array responses are the output. In this case, a large quantity of training data is required in order to cover the combinations and ranges of conductivities on the layer media. However, even if we use the technique developed for the efficient collection of training data (Ardjmandpour, 2010), it may not be practical to obtain sufficient data. To tackle this problem, one can use model reduction techniques to lessen memory and computational costs as demonstrated in this paper using the proper orthogonal decomposition (POD) method.

The POD method optimally extracts the fewest most energetic modes or basis functions from the numerical/experimental solutions that can accurately represent the system dynamic. POD was invented by Pearson (1901). Proper orthogonal decomposition is also known as principle component analysis (Kosambi, 1943; Fukunaga, 1990) in statistics, or Karhunen-Loève decomposition (Loève, 1945; Karhunen, 1946), and empirical orthogonal functions (EOF) in oceanography (Jolliffe, 2002; Crommelin and Majda, 2004) and meteorology (Majda et al., 2003).

The POD methodologies, in combination with the Galerkin projection procedure, have additionally provided an efficient means of generating reduced-order models (Holmes et al., 1998; Kunisch and Volkwein, 2003; Luo et al., 2007). This technique can provide a low dimensional ordinary differential equation (ODE) as an approximation to the PDE models. Basically the PDE's are solved for different parameter values to extract an ensemble of forward solutions, referred to as snapshots. The POD basis functions are obtained by applying a singular value decomposition (SVD) analysis to the snapshots. The Galerkin method is then used to project the PDE onto the reduced POD basis functions. To improve the accuracy of reduced models, a goal-oriented approach has been used to optimize the POD basis functions (Willcox et al., 2005; Bui-Thanh et al., 2007).

POD has been used successfully in several fields, such as fluid dynamics and coherent structures (Lumley, 1967; Aubry et al., 1988; Holmes et al., 1998; Willcox and Peraire, 2002), signal processing and pattern recognition (Fukunaga, 1990), image reconstruction (Kirby and Sirovich,

1990), inverse problems (Vauhkonen et al., 1997; Banks et al., 2000; Hopcroftand et al., 2009) and ocean modelling with the four-dimentional variational (4D-Var) data assimilation technique (Robert et al., 2005; Hoteit and Khl, 2006; Luo et al., 2007; Fang et al., 2009). In this paper, we propose to use the POD method for downhole measurements for the first time.

The COMSOL forward model [1] is used to generate snapshots, which are sampled at different conductivities. The solutions/snapshots, which are the azimuthal magnetic vector potentials, are stored in a data matrix, where each column represents the solution at each conductivity. The POD procedure is then used to extract the few most energetic modes/basis functions from the data matrix. The POD reduced model is then derived using Galerkin projection of the POD basis functions onto the governing equation used by COMSOL, which leads to the POD coefficients. Finally, the data matrix can be reconstructed with the use of the POD basis functions and coefficients. In order to construct the POD model, the numerical technique introduced by Fang et al. (2009, 2010) is used, whereby the POD forward model can be constructed by using the system matrices derived from the full model. The main advantages of POD are; i) it requires standard matrix computations and ii) it can applied to nonlinear problems (Schilders et al., 2008).

The POD basis functions are derived from snapshots using SVD. The POD basis functions are only able to give an optimal representation of the energy included in the snapshot sets. Therefore, the effectiveness of the POD basis rely on the generation of good snapshot sets (Gunzburger, 2003). Although, there are some methods such as the dual-weighed approach (Daescu and Navon, 2008; Chen et al., 2009) which can be used to select the snapshots, the choice and number of the snapshots are problem dependent and mostly rely on knowledge of the solution of the original physical system. In this study, snapshots are generated using a layered model in which the conductivity varies only with depth. The number of snapshots chosen is based on the fractional factorial design (Xu, 2005).

The reminder of this paper is structured as follows: In section 2, a brief introduction to the theory of array induction tools is given, followed by a brief description of the governing equations used in simulating the array induction tool responses. A brief review of POD is given in section 3. The reduced forward model is then derived, followed by a detailed description of mathematical procedure used to solve the POD model. Finally, the results are presented in section 4.

---

[1]http://www.comsol.com

2   Induction Tools

Fundamental aspects

Commercial induction tools are normally composed of several transmitter and receiver coils which are designed to optimize vertical resolution and depth of investigation. The basic element in an induction tool is the two-coil sonde, which consists of a transmitter and receiver mounted coaxially on a mandrel (Figure 1). The constant-amplitude alternating current in the transmitter coil sets up a primary electromagnetic field around the tool. The primary electromagnetic field induces eddy currents (often called "ground loops") in the formation. The eddy currents, which flow coaxially to the borehole and the intensity of which are proportional to conductivity of the formation, in turn induce a secondary voltage in a receiver coil. The voltage induced in the receiver directly from the transmitter coil is bucked-out using bucking coils, so that only the secondary voltages can be investigated.

The induced secondary voltage is due to the sum of all the eddy current loops with radius r, at depth z, weighted by geometrical factors to allow for their radial distance r from the borehole, and the vertical distance z above or below the transmitter. The induced secondary voltage is out-of-phase with the transmitter current, and therefore has both a real and an imaginary component. A complex conductivity for the formation can be obtained by dividing measured voltage by the K factor, which is a tool constant containing information about dimensions of transmitter and receiver (Moran and Kunz, 1962).

However, the measured signal is effected by the logging environment (Figure 2) such as

- Borehole effects: the conductivity of the mud and borehole size can affect the accuracy of the measurements; i.e. the influence of the borehole increases with mud conductivity and borehole diameter.

- Mud filtrate invasion: in permeable formations, responses are influenced by the spatial distribution of fluids/hydrocarbons in the vicinity of the borehole resulting from the invasion of mud filtrate.

- Shoulder effects: the conductivity/resistivity of the formation layers above and below a bed/layer of interest, referred as shoulder beds, can also effect the measurement.

- Dipping beds: the relative dip between the tool and formation can affect the tool responses, e.g. the effect of high relative dip angle is to blur the response and to introduce horns at the bed boundaries (Barber et al., 1999).

To accurately estimate the formation conductivity, one needs to correct the measurements for these effects. Traditional method for correction involved applying a series of corrections chart (Rust

and Anderson, 1975; Anderson, 2001; Hardman and Shen, 1987). However, the accuracy of the results largely relied on the experience of the log analyst. On the other hand, the manual corrections for the induction tools such as array tools (Hunka et al., 1990; Barber et al., 1995) with more measurements are time consuming. In the mid 1980's, the development of computer modelling made it possible for the log analyst to use correction algorithms based on forward modelling (Anderson, 2001).

Grove and Minerbo, in 1991, designed a correction algorithm to solve for borehole parameters by minimizing the difference between the model and measured signals from array induction tool. The borehole corrected signals are then combined to form the log responses which have the desired vertical response, radial response and a smooth near-borehole 2D response (Barber and Rosthal, 1991; Ellis and Singer, 2007). Then a 2D inversion can be used to estimate the formation conductivity and invasion parameters; i.e. invasion conductivity and invasion radius (Howard, 1992). In horizontal and deviated wells, the dip correction algorithms, based on filtering (Xiao et al., 2000) or iterative inversion (Barber et al., 1999) can be used to remove the dip effects.

However, the 2D inversion is slow because the nonlinearity of the problem leads to several iterations through the model for each interval. The process can be speeded up by dividing the problem into a sequence of 1D inverse problems, such as first determining vertical layers and then invasion depth (Lin et al., 1984; Dyos, 1987; Freedman and Minerbo, 1991; Anderson, 2001; Ellis and Singer, 2007). This can significantly reduce the computation time.

Assuming we can neglect invasion and dip effects, a 1D inversion can be used to estimate the conductivity in a layered medium. In this study, we introduce a fast surrogate model POD to predict the array response for a layered media. We demonstrate that the POD model is fast and accurate for an iterative inversion to estimate the formation conductivity. In this study the method is applied to the two-coil sonde. The method has been expanded for the multi array induction tool (Ardjmandpour, 2010).

Governing equation

COMSOL Multiphysics is a simulator software that uses Finite-Element models (FEM) to compute the array response. COMSOL uses a built-in formulation of the time harmonic Quasi-static electromagnetic equation. The partial differential equation, in 2D modelling, solved by COMSOL can be expressed as:

$$\left(i\omega\sigma - \omega^2\varepsilon_0\varepsilon_r\right)A_\phi + \nabla \times \left(\mu_0^{-1}\mu_r^{-1}\nabla \times A_\phi\right) = J_\phi^e, \tag{1}$$

where ω is the frequency of the current, μ_r is the relative magnetic permeability of the formation, σ is the formation conductivity, ε_0 is the dielectric permittivity of free space, ε_r is relative

dielectric permittivity, μ_0 is magnetic permeability of free space, A_ϕ is the azimuthal vector potential and J_ϕ^e is the azimuthal component of external current density.

The voltage induced in the receiver coils is computed using the relation, $E = i\omega A_\phi$. For a receiver coil of radius ρ with N_R turns, the induced voltage is calculated as follows:

$$V = 2\pi\rho N_R E = 2\pi\rho N_R i\omega A_\phi. \tag{2}$$

The discrete model of equation 1 can be written in a general form as follows:

$$E(\sigma)A_\phi = b, \tag{3}$$

where $E(\sigma)$ is the matrix including all the discretisation of equation 1 and b includes a discretised source term. The dimension of equation 3 is $N \times N$ where N is the number of grid points in the numerical model, e.g. for the data studied $N = 111081$. In the following subsections, we explain the mathematical procedure used to derive a low dimensional model of equation 3 using the POD approach.

3 POD reduced model

The solutions/snapshots obtained from the original full model are stored in the data matrix A with dimension $N \times K$, where K is the number of snapshots (typically $K \ll N$). The average of the ensemble of snapshots is defined as:

$$\bar{A}_i = \frac{1}{K} \sum_{k=1}^{K} A_{i,k}, \quad 1 \le i \le N. \tag{4}$$

Then, a new data matrix is formed by subtracting the mean $\bar{A}_i$ from each snapshot (Miranda et al., 2008):

$$C_{i,k} = A_{i,k} - \bar{A}_i. \tag{5}$$

The goal of POD is to find a set of orthogonal basis functions $\Phi = \Phi_1, \Phi_2, \cdots, \Phi_K$, such that it maximises:

$$\frac{1}{K}\sum_{k=1}^{K}\sum_{i=1}^{N}(C_{ik}\Phi_k)^2, \tag{6}$$

subject to:

$$\sum_{k=1}^{K}\Phi_k^2 = 1. \tag{7}$$

The optimal POD basis functions Φ_k are computed by forming the singular value decomposition (SVD) of the matrix $C \in R^{N \times K}$:

$$C = X\,\Delta\,U^T, \tag{8}$$

where diagonal entries of $\Delta = diag(\bar{\sigma}_1, \bar{\sigma}_2, \cdots, \bar{\sigma}_k)$ are the singular values, $X = (\Phi_1, \Phi_2, \cdots, \Phi_N)$ and, $U = (u_1, u_2, \cdots, u_K)$ are the matrices which consist of orthogonal vectors for CC^T and $C^T C$ respectively. In order to obtain the POD basis, we need to solve CC^T. This matrix has a dimension of $N \times N$, therefore an eigen decomposition of this matrix will be very computationally expensive. Therefore the $K \times K$ eigenvalue problem is solved as:

$$C^T C u_k = \lambda_k u_k; \quad 1 \le k \le K, \tag{9}$$

where $\lambda_k = \bar{\sigma}_k^2$ are real and positive and should be sorted in a descending order. In this case, the singular value decomposition is equivalent to the eigenvalue decomposition. The POD basis functions Φ are then calculated as follows:

$$\Phi_k = C_{ik}\,u_k/\sqrt{\lambda_k}. \tag{10}$$

The kth eigenvalue is a measure of the kinetic energy transferred within the kth basis mode (Fang et al., 2009). Since eigenvalues are arranged in descending order, we can choose the first M POD basis functions corresponding to the largest eigenvalues and neglect eigenvalues possessing small amounts of energy. The energy associated with the M basis functions can be quantified as $\mathcal{E}_M = \sum_{m=1}^{M}\lambda_m$. The total energy of the system is obtained by $\mathcal{E}_t = \sum_{k=1}^{K}\lambda_k$. The relative energy captured by the Mth basis functions is given by:

$$I(M) = \frac{\mathcal{E}_M}{\mathcal{E}_t}, \tag{11}$$

M can be chosen to capture the desired level of energy. There are other criteria which can be used to select M; e.g. the rate of decay of λ_k with increasing k, or through an iterative process by minimizing the error between the reduced order model and the full model (Cardoso and Durlofsky, 2010).

The POD basis functions are then used to reconstruct the data matrix as follows:

$$A_{i,k}^{POD} = \bar{A}_i + \sum_{m=1}^{M} \Phi_{i,m} \mathrm{a}_{m,k}, \tag{12}$$

where $\mathbf{a}$ are POD coefficients and are determined by solving the forward model in the reduced space. To calculate POD coefficients, we use the Galerkin projection, in which the POD basis functions are used as a basis to solve the full model. The procedure involves substituting the POD solution (equation 12) into the full forward model and taking the POD basis function as the test function, then integrating over the computational domain. The result of this procedure is a conductivity-dependent ordinary differential equation of an order equal to the number of the POD basis functions M. In this study, we solve the discrete representation of the ODE in which the system matrices are obtained by projecting the system matrices of the full forward model (E and b in equation 3) onto the POD basis. In the following subsections, each step of the approach will be explained in detail.

3.1 Discrete POD model for array induction measurement

The POD model is derived by substituting equation 12 into equation 1 and taking the POD basis function as the test function, then integrating over the computational domain, yielding:

$$\int_{\Omega} \Phi_j ((i\omega\sigma - \omega^2\varepsilon_0\varepsilon_r)(\bar{A} + \sum_{m=1}^{M} a_m \Phi_m(x)) +$$

$$\nabla \times (\mu_0^{-1}\mu_r^{-1}\nabla \times (\bar{A} + \sum_{m=1}^{M} a_m \Phi_m(x))) - J_\phi^e) d\Omega = 0, \tag{13}$$

where $\bar{A}$ is the mean value of the ensemble of snapshots, and in the finite element method, the POD basis $\Phi_m(x) = \sum_{i=1}^{N} \mathcal{N}_i \Phi_{mi}$. The discrete model of equation 13 can be written in a general form as:

$$\hat{E}(\sigma)\mathbf{a} = \hat{b}, \tag{14}$$

where $\hat{E}(\sigma)$ is the matrix including all the discretisation of equation 13 and $\hat{b}$ is including a discretised source term and the terms corresponding to the mean values (detailed explanation in section 3.2). $\hat{E}(\sigma)$ and $\hat{b}$ can be calculated by projecting E and b onto the basis functions as follows:

$$
\begin{aligned}
\hat{E}(\sigma) &= \Phi^T E(\sigma)\Phi, \\
\hat{b} &= \Phi^T b.
\end{aligned}
\tag{15}
$$

Therefore, the entry of the matrix $\hat{E}(\sigma)$ can be constructed by the entries of the matrix E (Fang et al., 2010) as:

$$\hat{E}_{ml}(\sigma) = \sum_{p=1}^{N}\sum_{q=1}^{N} E_{pq}(\sigma)\Phi_{m\,p}\Phi_{l\,q}, \tag{16}$$

$$\hat{b}_m = \sum_{p=1}^{N} b_p\Phi_{m\,p}, \tag{17}$$

where $E_{pq}(\sigma)$ is the $(p,q)^{th}$ entry of the matric E (equation 3) and b_p is the pth entry of b (equation 3).

In order to solve equation 14, one needs to derive the vector b and the system matrix $E(\sigma)$ for each value of conductivity. However, calculating $E(\sigma)$ for each value of conductivity, at each finite element and node over the computational domain is a time consuming process. To overcome this problem, we construct the matrix $E(\sigma)$ by a set of sub-matrices independent of conductivity, as follows (Fang et al., 2009, 2010):

$$E(\sigma) = E_0 + \sum_{l=1}^{L} \sigma^l(E_1^l - E_0), \tag{18}$$

where E_1^l and E_0 are derived from equation 1, when $\sigma = 1$ and $\sigma = 0$ respectively and l is the number of vertical layers considered in the model. Therefore, instead of calculating matrix E for each value of the conductivity, one needs to extract the sub-matrices E_0 and E_1 once prior to the POD calculations.

3.2 Forming the discrete POD model

This section explains how to solve the discrete POD model (equation 14). Since the forward model is complex, the discrete POD model is also complex, and can be written in a complex form as follows:

$$(\hat{P} + i\,\hat{Q})(\mathbf{a}_R + i\,\mathbf{a}_I) = (\hat{b}_R + i\,\hat{b}_I),$$

in a matrix form:

$$\begin{pmatrix} \hat{P} & -\hat{Q} \\ \hat{Q} & \hat{P} \end{pmatrix} \begin{pmatrix} \mathbf{a}_R \\ \mathbf{a}_I \end{pmatrix} = \begin{pmatrix} \hat{b}_R \\ \hat{b}_I \end{pmatrix}, \tag{19}$$

where $\hat{P}$ and $\hat{Q}$ are the real and imaginary parts of the matrix $\hat{E}$, respectively. The subscript $'R'$ refers to the real part and the subscript $'I'$ refers to the imaginary part.

To solve equation 19, first the POD basis functions are used to project the system to reduced space (equation 15). In order to obtain precise estimation of the complex solution, the POD basis are calculated for the real and imaginary parts separately. Therefore, the POD procedure is applied as follows:

- First, the data matrix C is constructed for the real and imaginary parts

$$\begin{aligned} C_R &= A_R - \bar{A}_R; & \text{real part,} \\ C_I &= A_I - \bar{A}_I; & \text{imaginary part,} \end{aligned} \tag{20}$$

  where A_R and A_I are the real and imaginary parts of the snapshots and $(\bar{A}_R)$ and $(\bar{A}_I)$ are the mean value of real and imaginary parts calculated using equation 4 respectively.

- Then the singular value decomposition is applied to C_R and C_I separately, leading to the POD basis for real (Φ_R) and imaginary (Φ_I) parts.

Once the POD basis functions (Φ_R and Φ_I) are obtained, the left hand side ($\hat{E}$) and the right hand side ($\hat{b}$) of equation 19 can be calculated as follows:

Calculating matrix $\hat{E}$

Considering equation 15:

$$\hat{E}(\sigma) = \Phi^T E(\sigma)\Phi, \tag{21}$$

Substituting $E = \begin{pmatrix} P & -Q \\ Q & P \end{pmatrix}$, where P and Q are the real and imaginary parts of the matrix E and POD basis functions $\Phi = \begin{pmatrix} \Phi_R & 0 \\ 0 & \Phi_I \end{pmatrix}$ in equation 21, yields:

$$\begin{pmatrix} \Phi_R^T P \Phi_R & -\Phi_R^T Q \Phi_I \\ \Phi_I^T Q \Phi_R & \Phi_I^T P \Phi_I \end{pmatrix}. \tag{22}$$

Taking into account equation 18, matrix $\hat{E}$ can be constructed as follows:

$$\begin{pmatrix} \Phi_R^T P_0 \Phi_R + \sum_{l=1}^{L} \sigma^l (\Phi_R^T P_1^l \Phi_R - \Phi_R^T P_0 \Phi_R) & -(\Phi_R^T Q_0 \Phi_I + \sum_{l=1}^{L} \sigma^l (\Phi_R^T Q_1^l \Phi_I - \Phi_R^T Q_0 \Phi_I)) \\ \Phi_I^T Q_0 \Phi_R + \sum_{l=1}^{L} \sigma^l (\Phi_I^T Q_1^l \Phi_R - \Phi_I^T Q_0 \Phi_R) & \Phi_I^T P_0 \Phi_I + \sum_{l=1}^{L} \sigma (\Phi_I^T P_1^l \Phi_I - \Phi_I^T P_0 \Phi_I) \end{pmatrix}, \tag{23}$$

where P_0 and Q_0 are the real and imaginary parts of E_0 and P_1 and Q_1 are the real and imaginary parts of E_1 respectively.

Calculating $\hat{b}$

The vector $\hat{b}$ includes a discretised source term and terms corresponding to the mean values is expressed as:

$$\hat{b} = \Phi^T (b - E(\sigma)\bar{A}), \tag{24}$$

The second term can be written in a matrix form as:

$$\begin{pmatrix} \Phi_R^T P \bar{A}_R - \Phi_R^T Q \bar{A}_I \\ \Phi_I^T Q \bar{A}_R + \Phi_I^T P \bar{A}_I \end{pmatrix} \quad \begin{matrix} \text{real part} \\ \text{imaginary part} \end{matrix} \tag{25}$$

The first term is real, therefore the equation 24 can be expressed as:

$$\begin{pmatrix} \Phi_R^T b - \Phi_R^T P \bar{A}_R + \Phi_R^T Q \bar{A}_I \\ -\Phi_I^T Q \bar{A}_R - \Phi_I^T P \bar{A}_I \end{pmatrix}. \tag{26}$$

Taking into account equation 18, the vector $\hat{b}$ can be constructed as follows:

$$
\begin{pmatrix}
\Phi_R^T b - \left(\Phi_R^T P_0 \bar{A}_R + \sum_{l=1}^L \sigma^l (\Phi_R^T P_1^l \bar{A}_R - \Phi_R^T P_0 \bar{A}_R)\right) + \left(\Phi_R^T Q_0 \bar{A}_I + \sum_{l=1}^L \sigma^l (\Phi_R^T Q_1^l \bar{A}_I - \Phi_R^T Q_0 \bar{A}_I)\right) \\
- \left(\Phi_I^T P_0 \bar{A}_I + \sum_{l=1}^L \sigma^l (\Phi_I^T P_1^l \bar{A}_I - \Phi_I^T P_0 \bar{A}_I)\right) - \left(\Phi_I^T Q_0 \bar{A}_R + \sum_{l=1}^L \sigma^l (\Phi_I^T Q_1^l \bar{A}_R - \Phi_I^T Q_0 \bar{A}_R)\right).
\end{pmatrix}
\tag{27}
$$

The coefficients $\mathbf{a}_I$ and $\mathbf{a}_R$ are then calculated by substituting equations 23 and 27 into equation 19. The dimension of the POD reduced model (equation 19) is $2M \times 2M$. Since $M \ll N$, the POD model has a much smaller dimension than the full model (equation 3).

To speed up the POD simulation, the sub-matrices; ($\Phi_R^T P_0 \Phi_R$, $\Phi_R^T P_1^l \Phi_R$, $\Phi_R^T Q_0 \Phi_I$, $\Phi_R^T Q_1^l \Phi_I$, $\Phi_I^T Q_0 \Phi_R$, $\Phi_I^T Q_1^l \Phi_R$, $\Phi_I^T P_0 \Phi_I$ and $\Phi_I^T P_1^l \Phi_I$) in equation 23 and ($\Phi_R^T P_0 \bar{A}$, $\Phi_R^T P_1^l \bar{A}$, $\Phi_R^T Q_0 \bar{A}_I$, $\Phi_R^T Q_1^l \bar{A}_I$, $\Phi_I^T P_0 \bar{A}_I$, $\Phi_I^T P_1^l \bar{A}_I$ and $\Phi_I^T Q_1^l$) in equation 27 are calculated once prior to the POD calculations; with a dimension of M which is much smaller than dimension N of P_0, Q_0, P_1 and Q_1. Therefore a POD simulation can be run in a few seconds. This significantly speeds up the POD calculation, especially in inverse problems, where the POD forward model needs to be run many times.

3.3 POD solution

The solution of the reduced order model $\mathbf{a}$ can then be converted back to a FE nodal vector by using the POD basis functions. The POD solution of the azimuthal vector potential for real and imaginary parts can be obtained as follows:

$$
\begin{aligned}
A_R^{POD}(x, \sigma) &= \bar{A}_R + \Phi_R^T \mathbf{a}_R; \qquad \text{real part,} \\
A_I^{POD}(x, \sigma) &= \bar{A}_I + \Phi_I^T \mathbf{a}_I; \qquad \text{imaginary part.}
\end{aligned}
\tag{28}
$$

4 Numerical experiments

In this section, the POD method is applied to the array induction measurements. Snapshots are generated by running COMSOL for different values of conductivities. The formation is modelled as a layered medium in which the conductivity varies only with depth. The POD basis functions are calculated based on singular value decomposition. The POD coefficients are calculated by solving the POD discrete model using the POD basis functions, leading to the reconstruction of the snapshots.

Generation of Snapshots

In order to generate the required snapshots for POD calculation, COMSOL simulation is used. A 5 layered model, as depicted in Figure 3, with the computational domain size $4m \times 2m$, with 10929 triangular elements and 111081 nodes in the model, is set up for array 1. We assume that there is no invasion and data has been corrected for borehole effect, therefore the borehole is not included in the model. The thickness of each layer is 0.07 m (3 inch). The transmitter coil (Tx) and main receiver (RxM) are located at the same distance from the center; the Tx coil is situated within the layer 2 and Main (RxM) and Bucking (RxB) coils are located 0.15 m and 0.1 m respectively from the source. The upper and lower sections of formation ("layer 0" and "layer 6") have a fixed background conductivity of 0.016 S/m. The solution is calculated as the azimuthal component of magnetic vector potential A_ϕ, the model imposes the Dirichlet boundary conditions $A_\phi = 0$ on the symmetry axis.

Snapshots are generated for different values of conductivities for each layer. The layer conductivities should be chosen in a way that can represent the values encountered in the actual formation, i.e. values between 0.001 S/m and 1 S/m. To achieve this, low (L), medium (M) and high (H) values of σ, in the range of 0.001-1 S/m, with the contrast 1:10 are chosen, i.e. L=0.001 S/m, M=0.03 S/m and H=1 S/m. The 27 combinations of L, M and H values of σ for 5 layers are chosen based on fractional factorial design (Xu, 2005). The design of 27 runs used to generate the snapshots is summarised in Table 1.

POD basis

The ensemble of snapshots C are constructed for the real and the imaginary parts (equation 20) separately. The ARPACK (Lehoucq et al., 1998), which is a collection of Fortran 77 subroutines that is designed to solve large scale eigenvalue problems, is then used to compute the eigenvalues and eigenvectors. Figure 4 shows the percentage energy (equation 11) captured by different numbers of POD basis functions. 5 POD basis functions can capture about 98% of the energy from the imaginary part and 86.68% from the real part. As can be seen, the more POD basis functions that are chosen, the better the % energy capture. The aim is to choose the minimum number of the POD basis which can capture most of the energy. In our case, 20 POD basis functions are chosen which can capture 99% of the energy from the real part and 99.99% of the energy from the imaginary part.

POD solution method

To solve the discrete POD model (section 3.2), the required system matrices (E_0 and E_1^l where $l = 1, 2, 3, \cdots, 5$) are derived from the full forward model as follows:

1. E_0 is obtained from discretization of equation 1 where the conductivity of all 5 layers is equal to zero.

2. E_1^1 is obtained where the conductivity corresponding to layer l is equal to 1 and other layers is equal to 0. For example for l=1 the conductivity of layer 1 is equal to 1 and layers 2 to 5 are equal to 0.

In total, the matrices $(E_0, E_1, E_2, E_3, E_4, E_5)$ and the vector b are extracted from the discretization of the full model (equation 1). These matrices and the vector b are used to construct $\hat{E}$ (equation 23) and $\hat{b}$ (equation 27), leading to solution of the discrete POD model (equation 14). The dimension of the reduced order model is 40, which is several orders of magnitude smaller than the dimension of the full model of 111081.

4.1 Results

Figures 5 to 8 show the POD solution of the azimuthal vector potential. Figures 5 and 6 illustrate the results for one of the snapshots which is used to calculate the POD basis functions (seen case) with conductivities of 0.03 S/m, 0.03 S/m, 0.001 S/m, 1 S/m, 0.001 S/m corresponding to layers 1 to 5 respectively. The results show that the POD solutions for both real and imaginary parts are in good agreement with those from the COMSOL. Figures 7 and 8 show the results of real and imaginary parts for a case, which is not used in determining the POD basis functions (we call it unseen case). The conductivities of each layer are 0.025 S/m, 0.033 S/m, 0.08 S/m, 0.09 S/m, and 0.09 S/m, from layers 1 to 5 respectively. The results for both seen and unseen cases show that the POD results agree well with those from the COMSOL. The maximum absolute difference errors between the COMSOL and POD solution, for both seen and unseen cases, are less than 0.4×10^{-11} S/m for real part and 0.4×10^{-12} S/m for imaginary part (Figures 5-c and 6-c). The close agreement between the forward and POD solutions on the unseen case validates the feasibility of the POD method.

To further quantify the quality of the POD results, voltages are calculated at Main and Bucking coils using the POD solution. The voltage of a coil can be calculated as follows (equation 2):

$$V = i\omega \frac{N_R}{h} \int_{line} 2\pi\rho A_\phi dz, \tag{29}$$

where h is the length of the coil and z is the vertical coordinate. The integral is taken over the line representing the cylindrical surface of the coil. The voltages in COMSOL are calculated using COMSOL interpolation and integration procedures.

In order to calculate V from the solution A_ϕ, without using COMSOL's interpolation, the mesh points situated on the coil surfaces are used. Each coil is represented by three points with the

coordinates of (ρ, z_1), (ρ, z_2) and (ρ, z_3). V is calculated using the value of A_ϕ at relevant mesh points as follows:

$$V = i2\pi\rho\omega\frac{N_R}{h}\left(\frac{1}{2}(A_\phi^1 + A_\phi^2)\Delta z_1 + \frac{1}{2}(A_\phi^2 + A_\phi^3)\Delta z_2\right), \tag{30}$$

where $\Delta z_1 = z_2 - z_1$ and $\Delta z_2 = z_3 - z_2$.

Figures 9 to 12 show real and imaginary parts of voltages of Main and Bucking coils for seen cases Table 1 with corresponding error E, which measures the difference between the voltages calculated using the forward model and the POD solutions. The results look very promising, with a good correlation between voltages calculated using POD and COMSOL solutions. As can be seen, for most of the cases the real part of voltages of the Main and Bucking coils can be estimated with an absolute error less than 0.5×10^{-4} S/m (for Main coil) and 0.5×10^{-6} S/m (for Bucking coil), with the maximum percentage error 6% for both Main and Bucking coils, however larger errors are observed for some cases such as 18 and 27, where most of layers have high conductivity (H=1 S/m). The imaginary part of the voltages for both Main and Bucking coils can be estimated with an absolute error less than 1.5×10^{-5} S/m (for Main coil) and 3.8×10^{-6} S/m (for Bucking coil), with a percentage error less than 1% for both Main and Bucking coils.

The results of calculated voltages for unseen cases (Table 2) are provided in Figures 13 to 16. Good correlation is again found between the calculated voltages from POD and COMSOL solutions, with absolute difference errors of less than 5×10^{-6} S/m for the real part and 2×10^{-6} for the imaginary part of Main and Bucking coils. The voltages of Main and Bucking coils can be estimated to within a 6% error on real and 1% error on imaginary parts.

5   Conclusions

In this paper, the POD method is introduced as a surrogate model to replace the computationally demanding COMSOL finite element model that solves Maxwell equations. First, the COMSOL forward model is run to obtain the solution snapshots at different conductivities. The POD basis functions are then calculated using singular value decomposition. The minimum number of POD basis functions, which can represent the maximum kinetic energy included in the snapshots, is chosen.

To solve the POD discrete model obtained from the full POD reduced model, a set of submatrices independent of conductivity is derived from discretization of the full model. These submatrices are then projected onto the reduced space by using the POD basis functions, leading to a discrete POD model of dimension M which is much smaller than dimension N of the full

forward model. In this way, a POD simulation can be run in a few seconds.

The POD model is applied to 27 snapshots obtained from COMSOL using a 5-layer model. The layer conductivities are chosen from a combination of three values of conductivities, 0.001 S/m, 0.03 S/m and 1 S/m, based on fractional factorial design. The 27 snapshots with 20 POD basis functions, for each real and imaginary parts, are chosen to capture more than 99% of the energy of the real part and 99.99% of the energy of the imaginary part.

The results obtained from seen and unseen cases show that the POD solutions agree well with the ones obtained from the forward model for both real and imaginary parts. Evaluation of the accuracy of the POD model is also carried out through the calculation of voltages using the POD solutions. The close agreement between voltages estimated from COMSOL and POD solutions, for both seen and unseen cases, validates the accuracy of POD solutions. Overall, the results show that the POD method is fast and accurate and thus may be a good candidate for future formation conductivity inversion in a layered media.

REFERENCES

Anderson, B. and Gianzero, S. (1983). Induction sonde response in stratified media. *The Log Analyst*, 24(1):25–31.

Anderson, B. I. (2001). *Modeling and Inversion Methods for the Interpretation of Resistivity Logging Tool Response*. PhD thesis, Technische Universiteit Delft.

Ardjmandpour, N. (2010). *MOdelling and Inversion of Array Induction Tool*. PhD thesis, Imperial College London.

Aubry, N., Holmes, P., and Lumley, J. L. (1988). The dynamics of coherent structures in the wall region of a turbulent boundary layer. *Journal of Fluid Dynamics*, 192:115–173.

Banks, H. T., Joyner, M. L., Wincheski, B., and Winfree, W. P. (2000). Nondestructive evaluation using a reduced-order computational methodology. *Inverse Problems*, 16(4):929–945.

Barber, T., Orban, A., Hazen, G., Long, T., Schlein, R., Alderman, S., Tabanou, J., and Seydoux, J. (1995). A multiarray induction tool optimized for efficient wellsite operation. *SPE Annual Technical Conference and Exhibition, 22-25 October 1995, Dallas, Texas*, SPE 30583.

Barber, T. D., Broussard, T., Minerbo, G. N., Murgatroyd, D., and Sijercic, Z. (1999). Interpretation of multiarray induction logs in invaded formations at high relative dip angles. 40(3):220–217.

Barber, T. D. and Rosthal, R. A. (1991). Using a multiarray induction tool to achieve high-resolution logs with minimum environmental effects. *SPE Annual Technical Conference and Exhibition, Dallas, Texas.*

Bui-Thanh, T., Willcox, K., Ghattas, O., and van Bloemen Waanders, B. (2007). Goal-oriented, model-constrained optimization for reduction of large-scale systems. *J. Comput. Phys.*, 224:880–896.

Cardoso, M. A. and Durlofsky, L. J. (2010). Linearized reduced-order models for subsurface flow simulation. *J. Comput. Phys.*, 229(3):681–700.

Chen, X., Navon, I. M., and Fang, F. (2009). A dual-weighted trust-region adaptive POD 4D-VAR applied to a finite-element shallow-water equations model. *International Journal for Numerical Methods in Fluids*.

Crommelin, D. T. and Majda, A. J. (2004). Strategies for model reduction: Comparing different optimal bases. *Journal of the Atmospheric Sciences*, 61(17):2206–2217.

Daescu, D. N. and Navon, I. M. (2008). A Dual-Weighted approach to order reduction in 4DVAR data assimilation. *Monthly Weather Review*, 136(3):1026–1041.

Doll, H. G. (1949). Introduction to induction logging and application to logging of wells drilled with oil base mud. *Journal of Petroleum Technology*, 1:148–162.

Dyos, C. J. (1987). Inversion of induction log data by the method of maximum entropy. *In SPWLA 28th Annual Logging Symposium Transactions. Society of Professional Well Log Analysts*, July 1-13.

Ellis, D. V. and Singer, J. M. (2007). *Well logging for Earth Scientists*. Springer, The Netherlands.

Fang, F., Pain, C. C., Navon, I. M., Gorman, G. J., Piggott, M. D., and Allison, P. A. (2010). The independent set perturbation adjoint method: A new method of differentiating mesh-based fluids models. *International Journal for Numerical Methods in Fluids*.

Fang, F., Pain, C. C., Navon, I. M., Piggott, M. D., Gorman, G. J., Allison, P. A., and Goddard, A. J. H. (2009). Reduced order modelling of an adaptive mesh ocean model. *International Journal for Numerical Methods in Fluids*, 59:827–851.

Freedman, R. and Minerbo, G. N. (1991). Maximum Entropy Inversion of Induction-Log Data. *SPE Formation Evaluation*, 6:259–268.

Fukunaga, K. (1990). *ntroduction to Statistical Recognition (2nd edn). Computer Science and Scientific Coomputing Series.* Academic Press: Boston, MA.

Grove, G. P. and Minerbo, G. N. (1991). An adaptive borehole correction scheme for array induction tools. *Society of Professional Well Log Analysts Logging Symposium*, Paper P:1–25.

Gunzburger, M. D. (2003). *Perspectives in flow control and optimization*. SIAM.

Hardman, R. H. and Shen, L. C. (1987). Charts for correcting the effect of formation dip and hole deviation on induction logs. 28(4):349–356.

Holmes, P., Lumley, J. L., and Berkooz, G. (1998). *Turbulence Coherent Structures, Dynamical Systems and Symmetry*, volume 192.

Hopcroftand, P. O., Gallagher, K., Pain, C. C., and Fang, F. (2009). Three-dimensional simulation and inversion of borehole temperatures for reconstructing past climate in complex settings. *J. Geophys. Res.*, 114.

Hoteit, I. and Khl, A. (2006). Efficiency of reduced-order, time-dependent adjoint data assimilation approaches. *Journal of Oceanography*, 62:539–550.

Howard, A. Q. (1992). A new invasion model for resistivity log interpretation. *Log Analyst*, 33(2):96–110.

Hunka, J., Barber, T. D., Rosthal, R. A., Minerbo, G. N., Head, E. A., Howard, A., Hazen, G., and Chandler., R. (1990). A new resistivity measurement system for deep formation imaging and high-resolution formation evaluation. In *Proceedings 1990 SPE Annual Technical Conference and Exhibition.*, volume SPE 20559. Society of Petroleum Engineers.

Jolliffe, I. T. (2002). *Principal Component Analysis*. Springer, second edition.

Karhunen, K. (1946). Zur spektraltheorie stochastischer prozesse. *Annales Academi Scientiarum Fennic*, 34:1–7.

Kirby, M. and Sirovich, L. (1990). Application of the KarhunenLoève procedure for the characterization of human faces. *IEEE Transactions on Pattern Analysis and Machine Intelligence*, 12:103 – 108.

Kosambi, D. D. (1943). Statistics in function space. *Journal of the Indian Mathematical Society*, 7:76 – 88.

Kunisch, K. and Volkwein, S. (2003). Galerkin proper orthogonal decomposition methods for a general equation in fluid dynamics. *SIAM Journal on Numerical Analysis*, 40(2):492–515.

Lehoucq, R. B., Sorensen, D. C., and Yang, C. (1998). *ARPACK Users' Guide: Solution of Large-Scale Eigenvalue Problems with Implicitly Restarted Arnoldi Methods*. Siam.

Lin, Y.-Y., Gianzera, S., and Strickland, R. (1984). Inversion of induction logging data using the least squares technique. *In SPWLA 25th Annual Logging Symposium Transactions. Society of Professional Well Log Analysts*, June 10-13.

Loève, M. (1945). Sur les fonctions aleatoires stationaires du second ordre. *Revue Scientifique*, 83:297–303.

Lumley, J. L. (1967). The structure of inhomogeneous turbulence. *Atmospheric Turbulence and Wave Propagation*, pages 166 – 178.

Luo, Z., Zhu, J., Wang, R., and Navon, I. M. (2007). Proper orthogonal decomposition approach and error estimation of mixed finite element methods for the tropical pacific ocean reduced gravity model. *Computer Methods in Applied Mechanics and Engineering*, 196(41-44):4184–4195.

Majda, A. J., Timofeyev, I., and Vanden-Eijnden, E. (2003). Systematic strategies for stochastic mode reduction in climate. *Journal of the Atmospheric Sciences*, 60(14):1705–1722.

Miranda, A., Le Borgne, Y.-A., and Bontempi, G. (2008). New routes from minimal approximation error to principal components. *Neural Processing Letters*, 27:197–207.

Moran, J. H. (1982). Induction logging-geometrical factors with skin effect. *The Log Analyst*, 23(6):4 – 10.

Moran, J. H. and Kunz, K. S. (1962). Basic theory of induction logging and application to study of two-coil sondes. *Geophysics*, 27(6):829–858.

Pearson, K. (1901). On lines and planes of closest fit to systems of points in space. 2(6):559572.

Robert, C., Durbiano, S., Blayo, E., Verron, J., Blum, J., and Dimet, F.-X. L. (2005). A reduced-order strategy for 4d-var data assimilation. *Journal of Marine Systems*, 57(1-2):70 – 82.

Rust, D. and Anderson, B. (1975). An intimate look at induction logging. Technical Reniew 2.

Schilders, W. H. A., van der Vorst, H. A., and Rommes, J. (2008). *Model order reduction: theory, research aspects and applications*, volume 13. Springer ECMI Series on Mathematics in Industry.

Thadani, S. G., Merchant, G. A., and Verbout, J. L. (1983). Deconvolution with variable frequency induction logging systems. *SPWLA Twenty Fourth Annual Logging Symposium*, June 27-30.

Vauhkonen, M., Kaipio, J. P., Somersalo, E., and Karjalainen, P. A. (1997). Electrical impedance tomography with basis constraints. *Inverse Problems*, 13(2):523–530.

Willcox, K., Ghattas, O., van Bloemen Waanders, B., and Bader, B. (2005). An optimization framework for goal-oriented, model-based reduction of large-scale systems.

Willcox, K. and Peraire, J. (2002). Balanced model reduction via the proper orthogonal decomposition. *AIAA Journal*, 40:2323 – 2330.

Xiao, J., Geldmacher, I., and Rabinovich, M. (2000). Deviated-well software focusing of multiarray induction measurements. *SPWLA* 41th *Annual Logging Symposium*, June 4-7.

Xu, H. (2005). A catalogue of three-level regular fractional factorial designs. *Metrika*, 62(2):259–281.

List of Figures

No of Cases	Layer 1	Layer 2	Layer3	Layer 4	Layer 5
1	0.001	0.001	0.001	0.001	0.001
2	0.001	0.001	0.03	0.03	0.001
3	0.001	0.001	1	1	0.001
4	0.001	0.03	0.001	0.03	1
5	0.001	0.03	0.03	1	1
6	0.001	0.03	1	0.001	1
7	0.001	1	0.001	1	0.03
8	0.001	1	0.03	0.001	0.03
9	0.001	1	1	0.03	0.03
10	0.03	0.001	0.001	0.03	0.03
11	0.03	0.001	0.03	1	0.03
12	0.03	0.001	1	0.001	0.03
13	0.03	0.03	0.001	1	0.001
14	0.03	0.03	0.03	0.001	0.001
15	0.03	0.03	1	0.03	0.001
16	0.03	1	1	0.001	1
17	0.03	1	0.03	0.03	1
18	0.03	1	1	1	1
19	1	0.001	0.001	1	1
20	1	0.001	0.03	0.001	1
21	1	0.001	1	0.03	1
22	1	0.03	0.001	1	0.03
23	1	0.03	1	0.03	0.03
24	1	0.03	1	1	0.03
25	1	1	0.001	0.03	0.001
26	1	1	1	1	0.001
27	1	1	0.001	0.001	0.001

Table 1: The 27 best runs of 3 values of conductivities (0.001 S/m, 0.03 S/m and 1 S/m) for 5 layers determined based on the fractional factorial design (Xu, 2005).

No of Cases	Layer 1	Layer 2	Layer3	Layer 4	Layer 5
1	0.25	0.25	0.25	0.25	0.25
2	0.25	0.22	0.05	0.025	0.025
3	0.05	0.025	0.025	0.025	0.025
4	0.025	0.025	0.025	0.025	0.025
5	0.025	0.025	0.03	0.08	0.09
6	0.03	0.08	0.09	0.09	0.09
7	0.09	0.09	0.09	0.09	0.09
8	0.08	0.03	0.025	0.025	0.025
9	0.03	0.025	0.025	0.025	0.025
10	0.025	0.025	0.025	0.015	0.014
11	0.025	0.023	0.015	0.014	0.014
12	0.023	0.015	0.014	0.014	0.014
13	0.015	0.014	0.014	0.014	0.014
14	0.014	0.03	0.17	0.2	0.2
15	0.03	0.17	0.2	0.2	0.2
16	0.017	0.2	0.2	0.2	0.2
17	0.2	0.2	0.2	0.2	0.2
18	0.2	0.2	0.2	0.19	0.17
19	0.2	0.2	0.19	0.17	0.16
20	0.2	0.19	0.17	0.16	0.16
21	0.19	0.17	0.16	0.16	0.16
22	0.17	0.16	0.16	0.16	0.16

Table 2: The conductivity of the each layer for unseen cases.
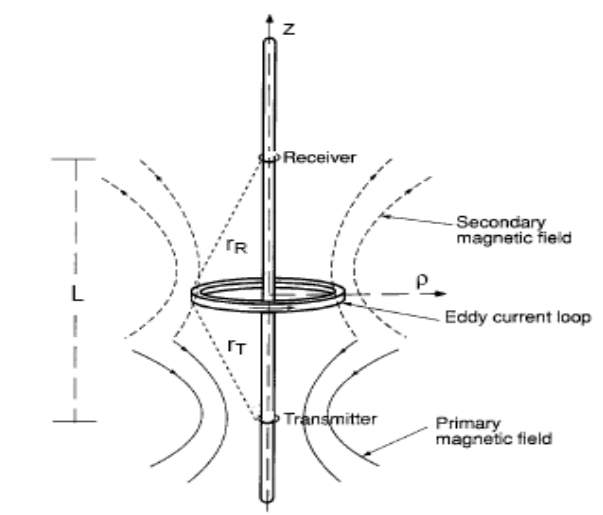
Figure 1: Basic two-coil induction tool. The vertical component of the magnetic field from the transmitter coil induces ground loop currents. The current loops in the conductive formation produce a secondary magnetic field detected by the receiver coil (Anderson, 2001).
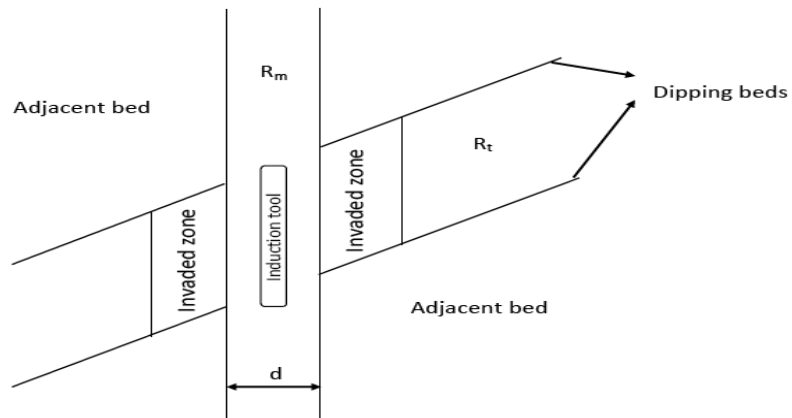
Figure 2: The logging environment such as mud conductivity and borehole size, mud filtrate invasion, adjacent bed and dipping beds affect on the measured signal. To estimate the true formation conductivity, one needs to correct for these effects.
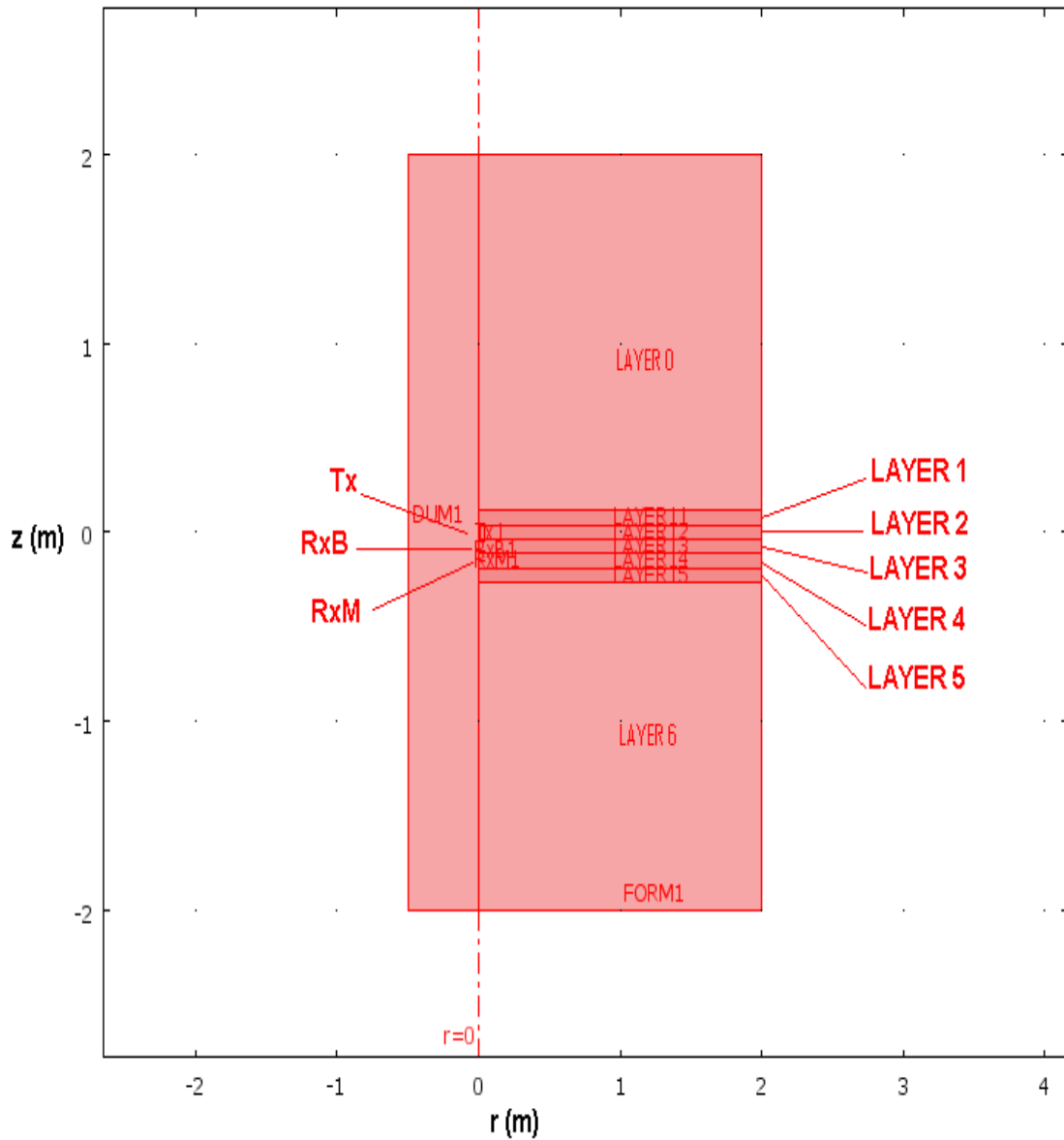
Figure 3: Layered media to be modelled to generate the required snapshots for POD model reduction. We assume that the data are borehole corrected, therefore the borehole is not included in the model. Layer thickness (layers 1 to 5) is 0.07 m (3 inch). The transmitter coil (Tx) is situated within layer 2 and Main (RxM) and Bucking (RxB) coils are located 0.15 m (6 inch) and 0.1 m (4 inch) respectively form Tx. The solution is calculated as the azimuthal component of magnetic vector potential A_ϕ, the model imposes the Dirichlet boundary conditions $A_\phi = 0$ on the symmetry axis.
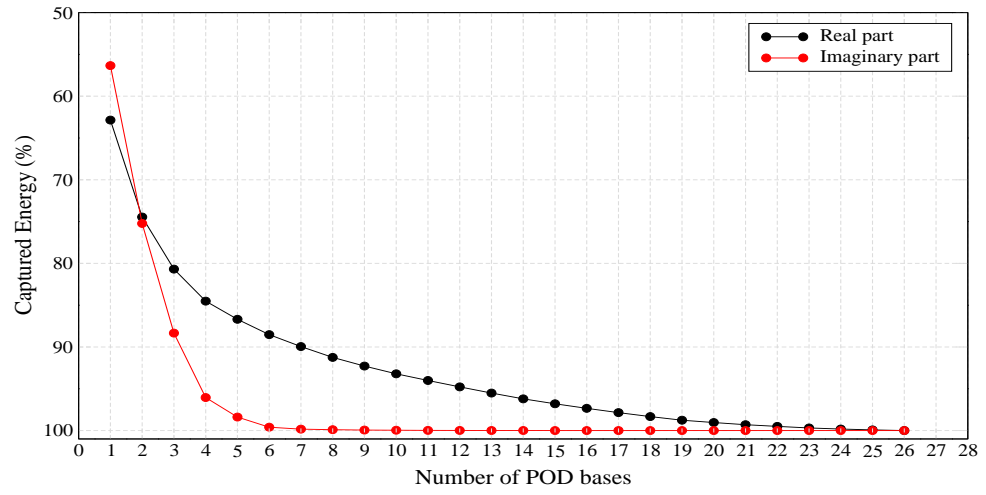
(a)

Figure 4: Energy percentage captured by POD basis for real and imaginary parts. In our case, we choose 20 POD basis functions which can capture 99% energy from the real part and 99.99% energy from the imaginary part.
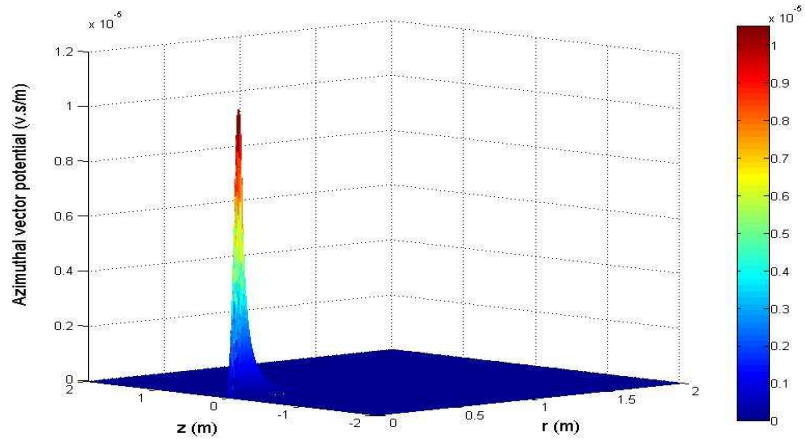
(a) COMSOL solution
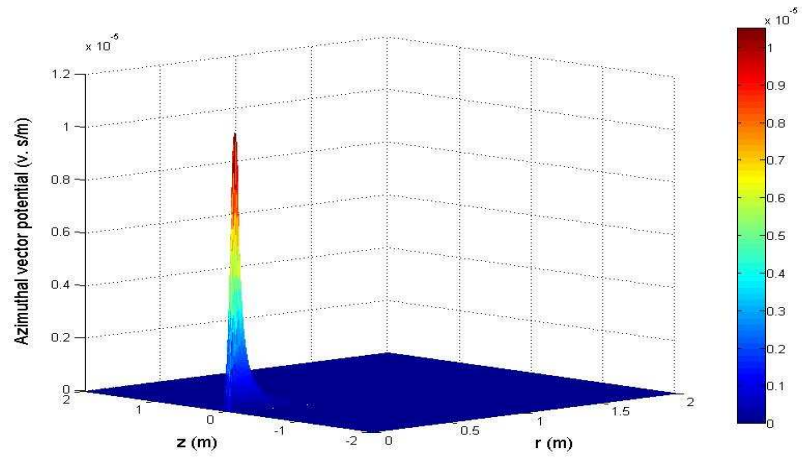
(b) POD solution
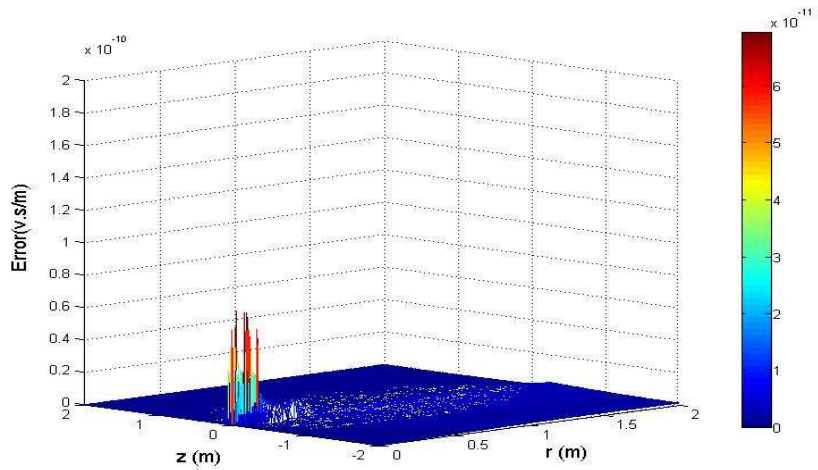
(c) Error

Figure 5: Comparison of the real part of azimuthal vector potential between the full model (a) and the reduced model (b) for a seen case with conductivities of 0.03 (S/m), 0.03 (S/m), 0.001 (S/m), 1 (S/m), 0.001 (S/m) for each layer. c) The error between the forward and POD solution.
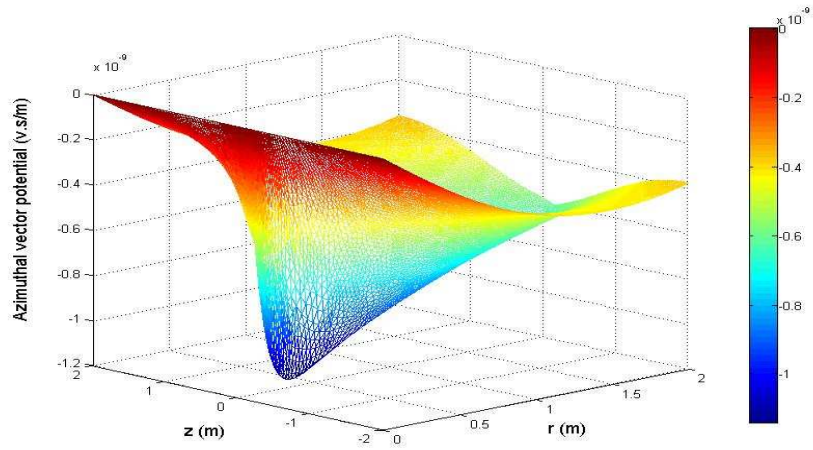
(a) COMSOL solution
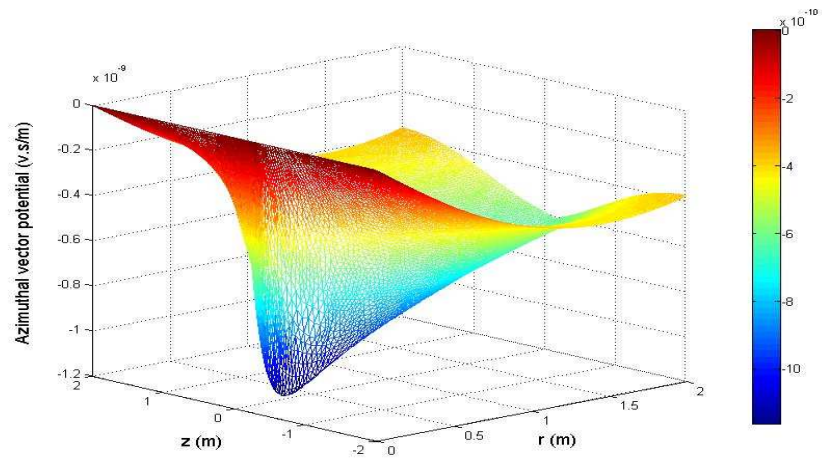
(b) POD solution
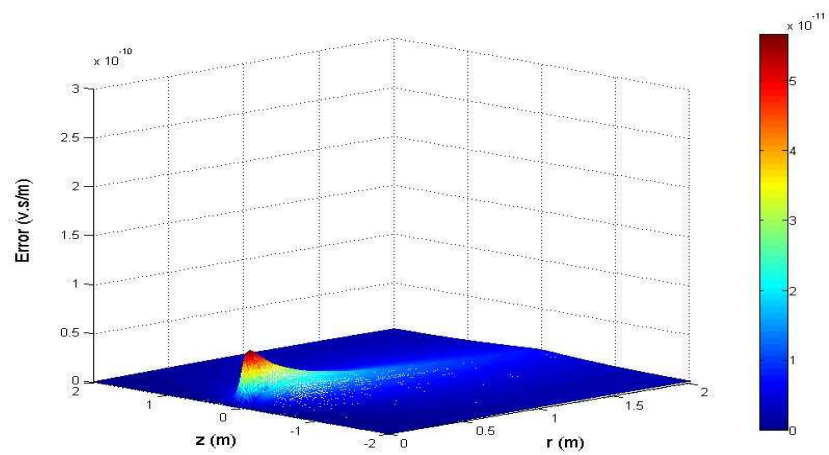
(c) Error

Figure 6: Comparison of the imaginary part of azimuthal vector potential between the full model (a) and the reduced model (b) for a seen case with conductivities of 0.03 (S/m), 0.03 (S/m), 0.001 (S/m), 1 (S/m), 0.001 (S/m) for each layer. c) The error between the forward and POD solution.
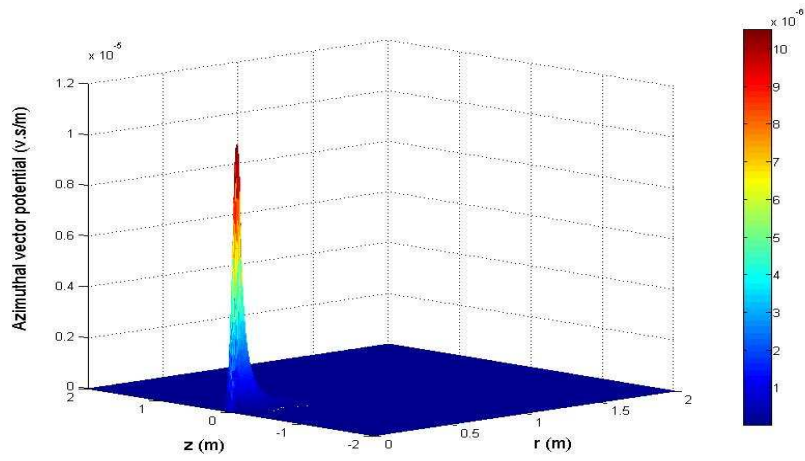
(a) COMSOL solution
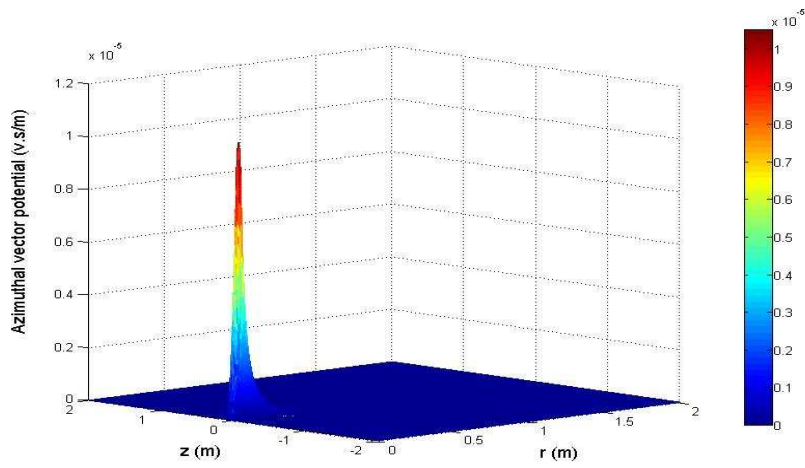
(b) POD solution
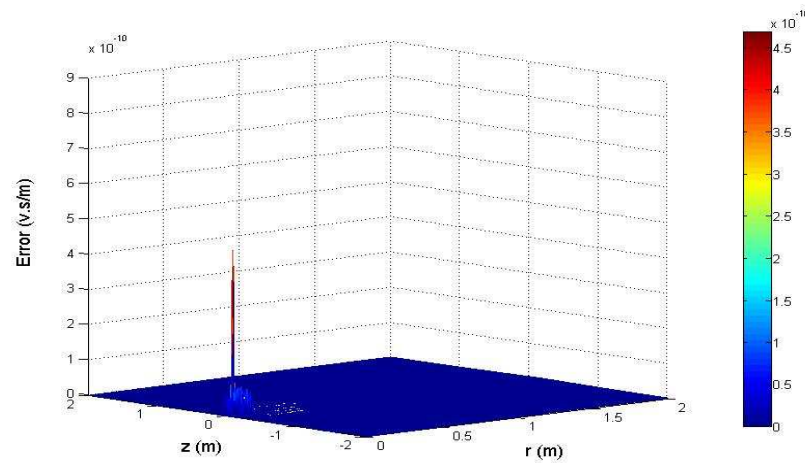
(c) Error

Figure 7: Comparison of the real part of azimuthal vector potential between the full model (a) and the reduced model (b) for an unseen case with conductivities of 0.025 (S/m), 0.033 (S/m), 0.08 (S/m), 0.09 (S/m), 0.09 (S/m) for each layer. c) The error between the forward and POD solution.
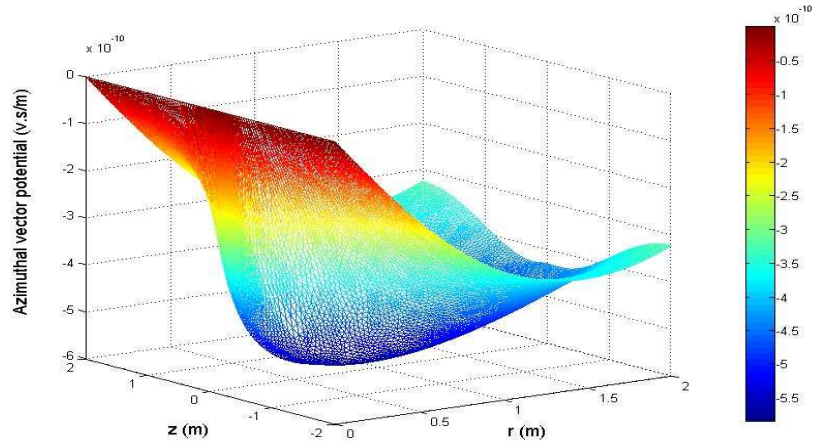
(a) COMSOL solution
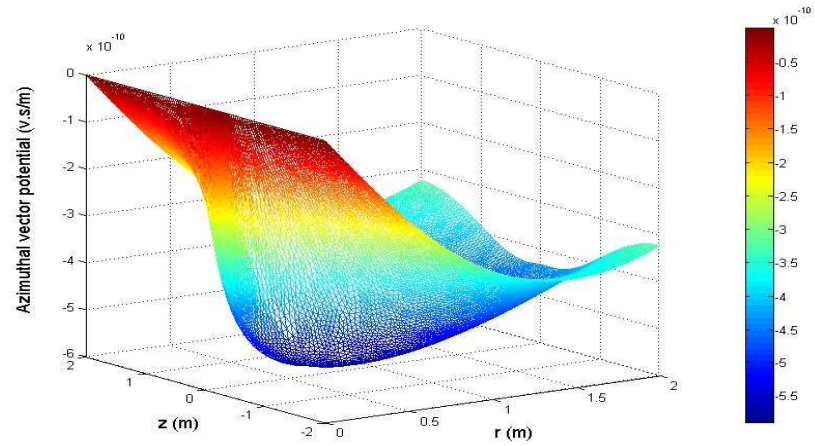
(b) POD solution
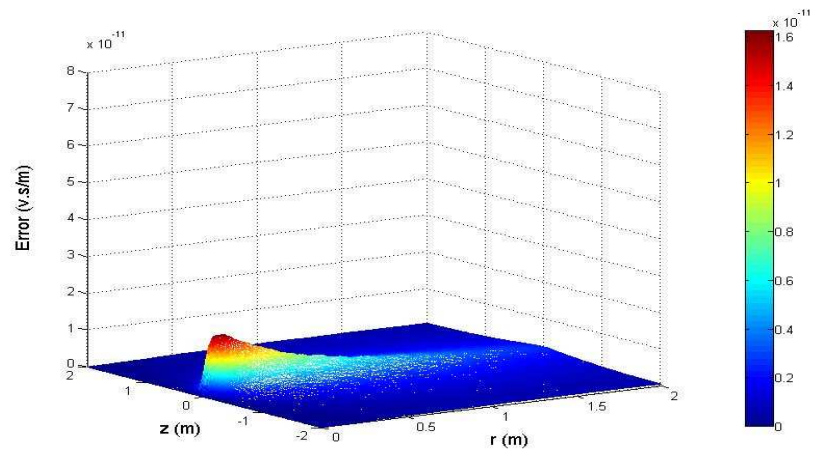
(c) Error

Figure 8: Comparison of the imaginary part of azimuthal vector potential between the full model (a) and the reduced model (b) for an unseen case with conductivities of 0.025 (S/m), 0.033 (S/m), 0.08 (S/m), 0.09 (S/m), 0.09 (S/m) for each layer. c) The error between the forward and POD solution.
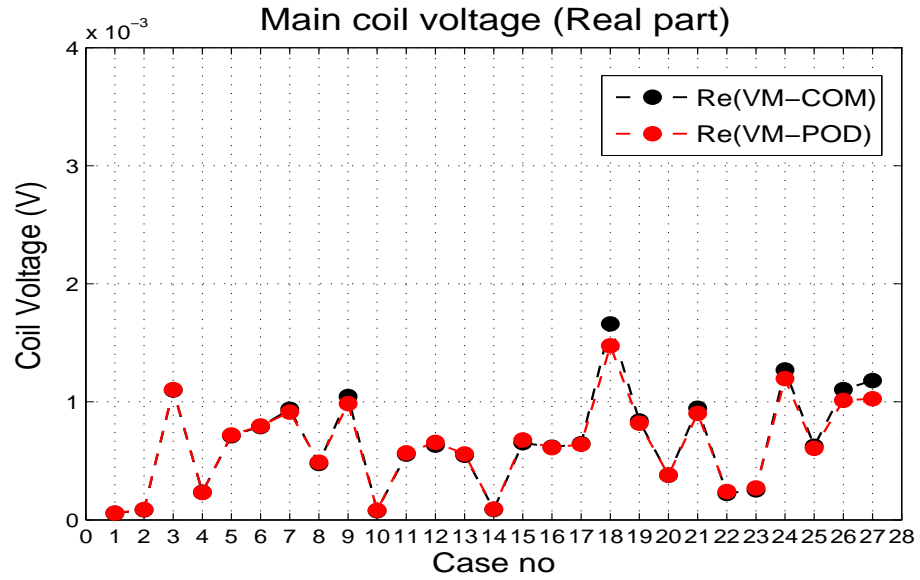
(a)
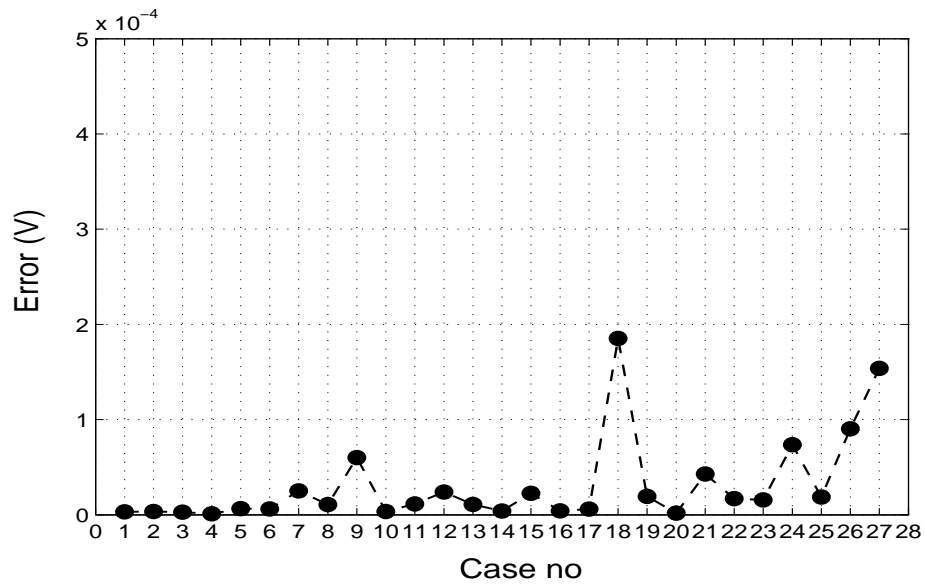
(b)

Figure 9: a) Comparison between the real part of the voltages of Main coil calculated from COMSOL and POD solutions for 27 snapshots (Table 1) that are used to obtain the POD basis functions. b) the absolute error ($E = |Vm^R_{COM} - Vm^R_{POD}|$).
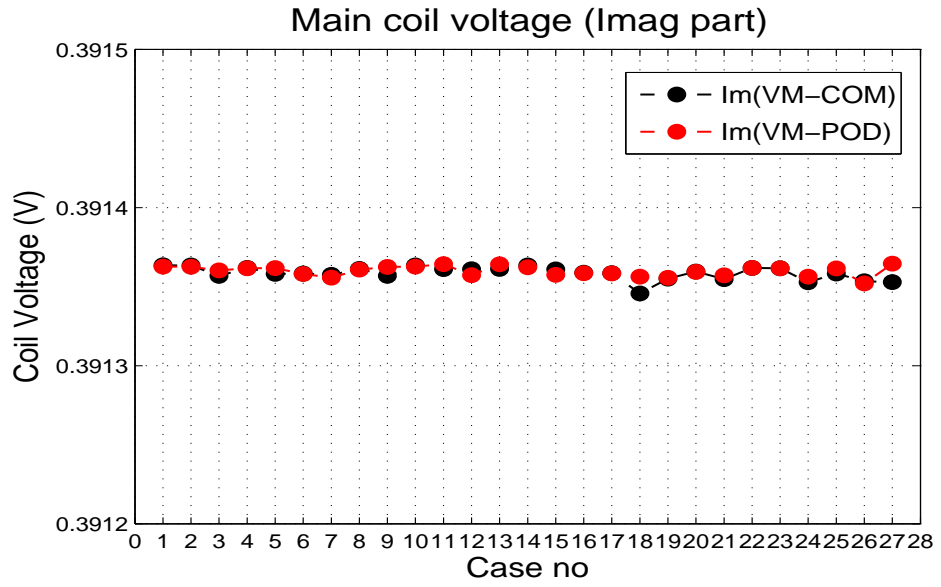
(a)
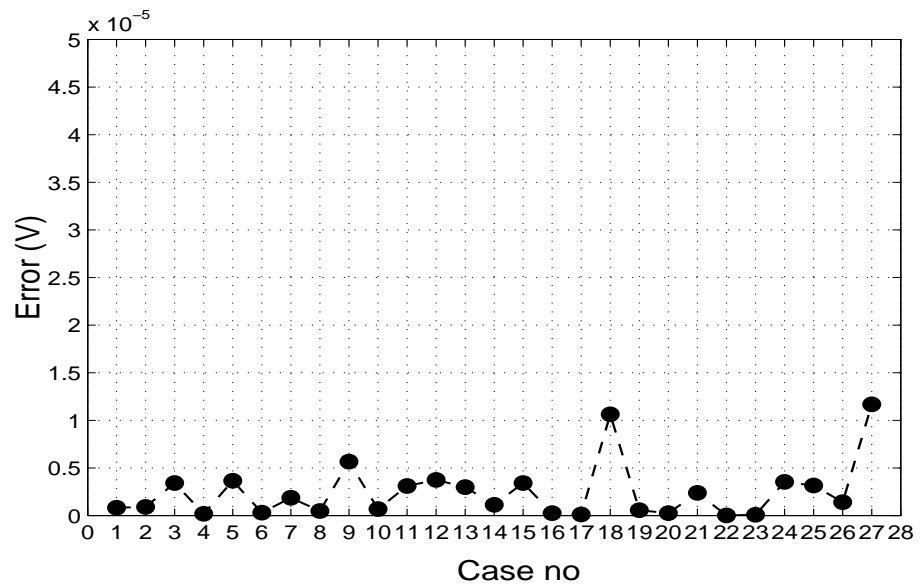
(b)

Figure 10: a) Comparison between the imaginary part of the voltages of Main coil calculated from COMSOL and POD solutions for 27 snapshots (Table 1) that are used to obtain the POD basis functions. b) the absolute error ($E = |Vm_{COM}^I - Vm_{POD}^I|$).
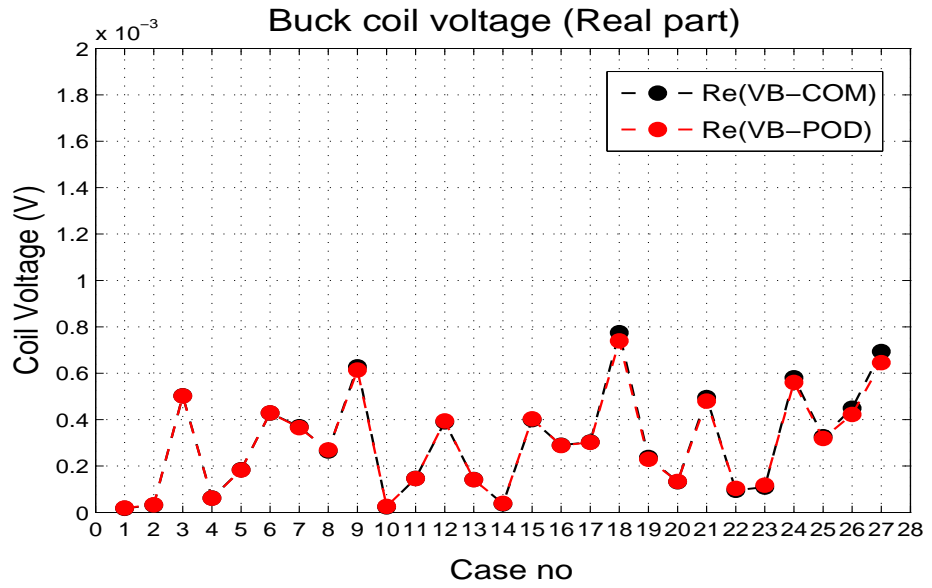
(a)
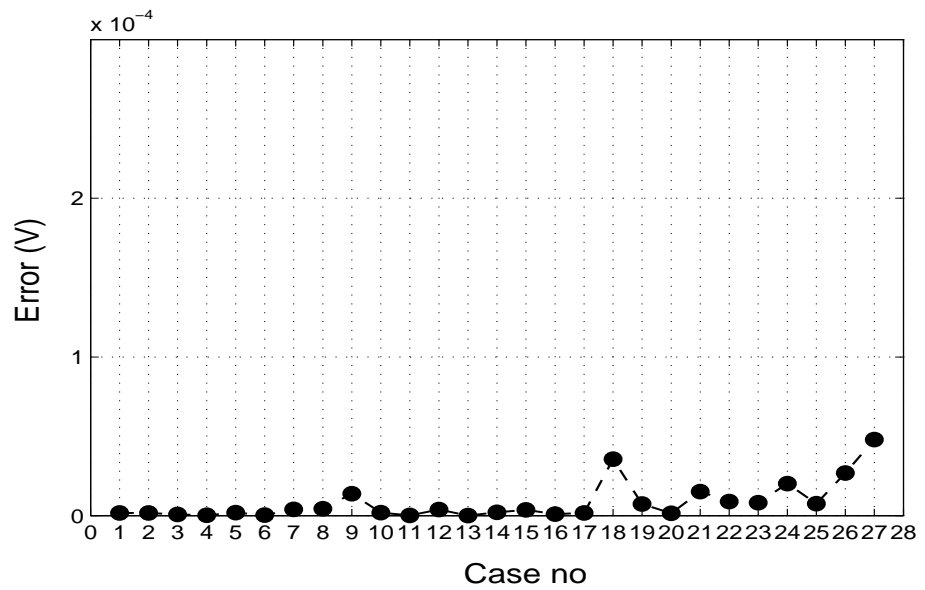
(b)

Figure 11: a) Comparison between the real part of voltages of Bucking coil calculated from COMSOL and POD solutions using equation for 27 snapshots (Table 1) that are used to obtain the POD basis functions. b) the absolute error between the estimated voltages from POD and COMSOL solution.
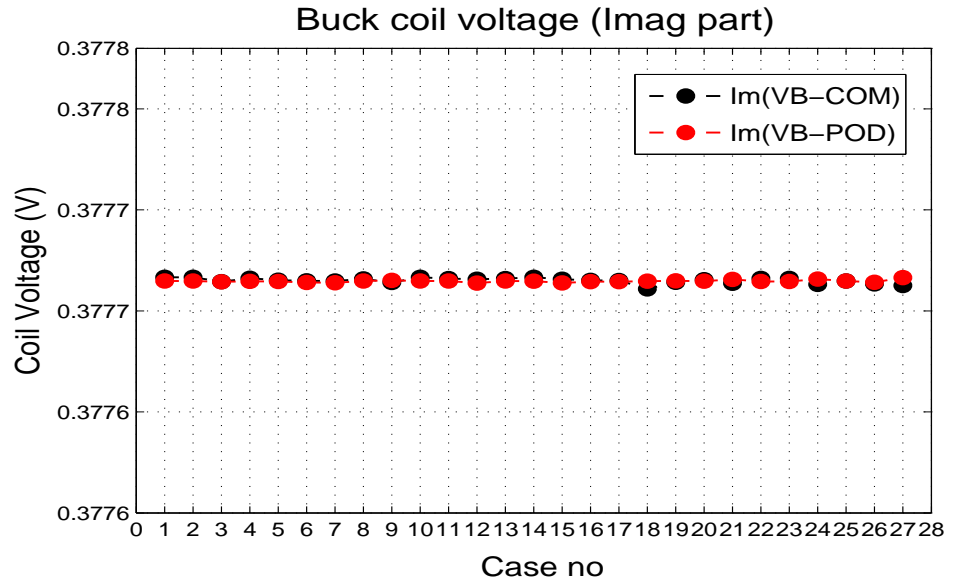
(a)
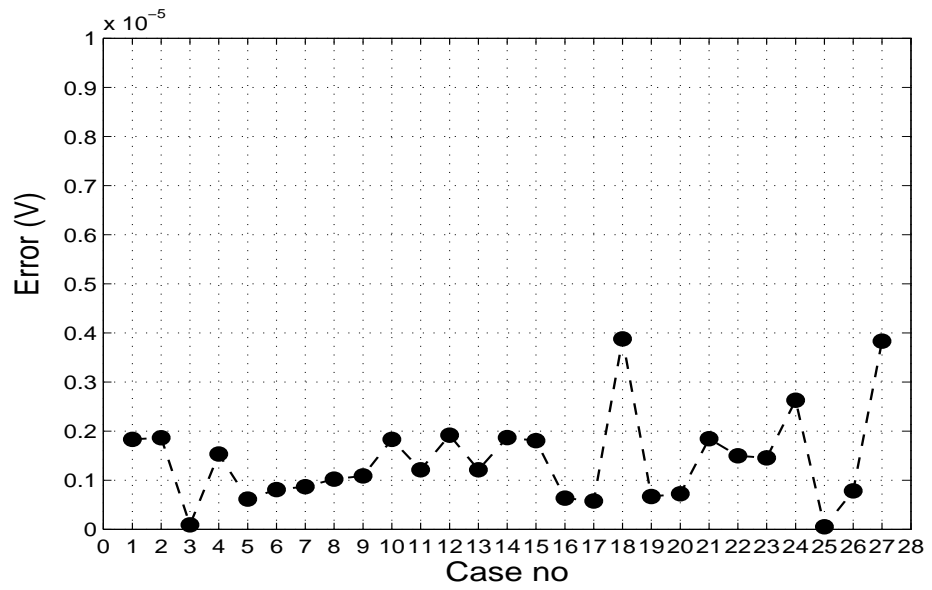
(b)

Figure 12: a) Comparison between the imaginary part of voltages of Bucking coil calculated from COMSOL and POD solutions for 27 snapshots (Table 1) that are used to obtain the POD basis functions. b) the absolute error between the estimated voltages from POD and COMSOL solution.
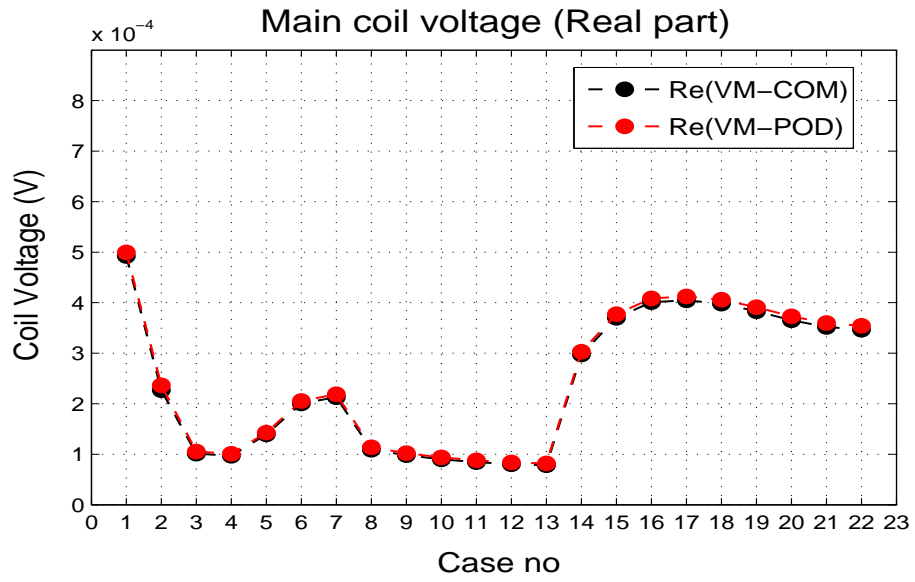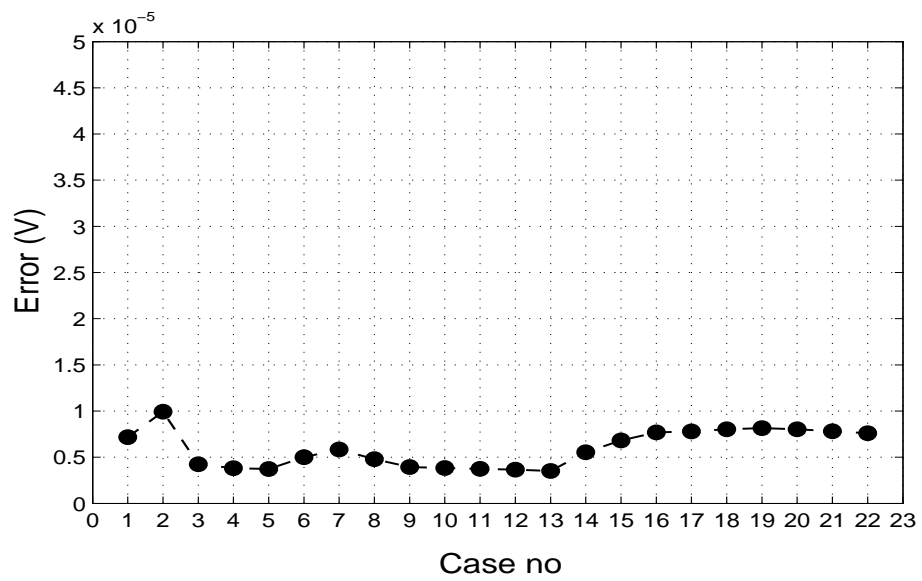
Figure 13: a) Comparison between the real part of the voltages of Main coil calculated from COMSOL and POD solutions for unseen cases (Table 2). b) the absolute error between the calculated voltages from POD and COMSOL solution is less than 1×10^{-5} S/m for most of the cases.
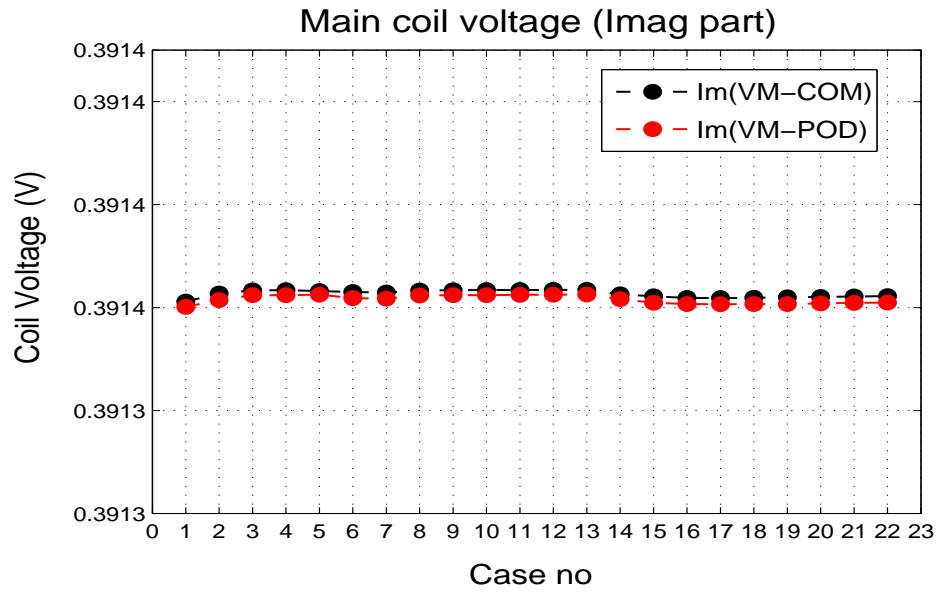
(a)
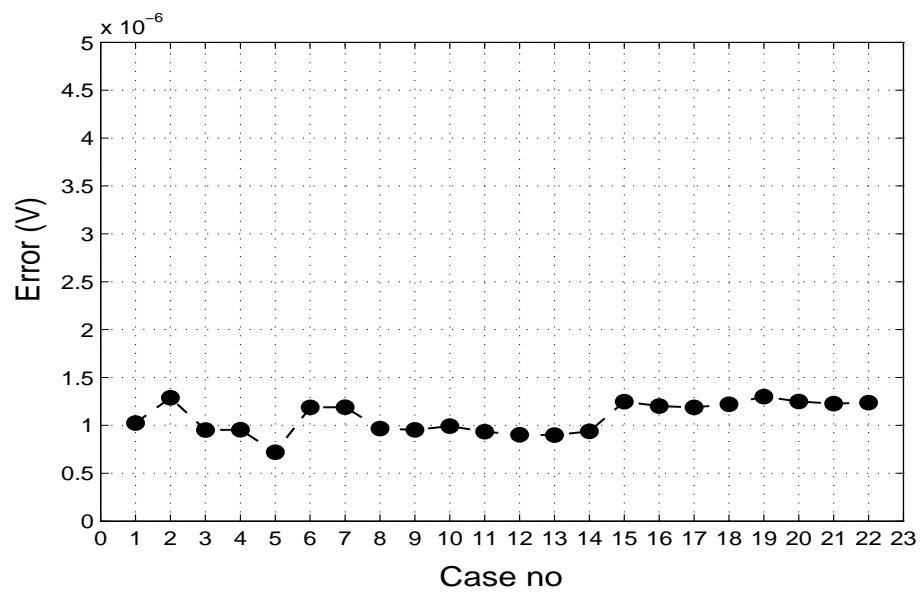
(b)

Figure 14: a) Comparison between the imaginary part of the voltages of Main coil calculated from COMSOL and POD solutions for unseen cases (Table 2). b) the absolute error between the calculated voltages from POD and COMSOL solution.
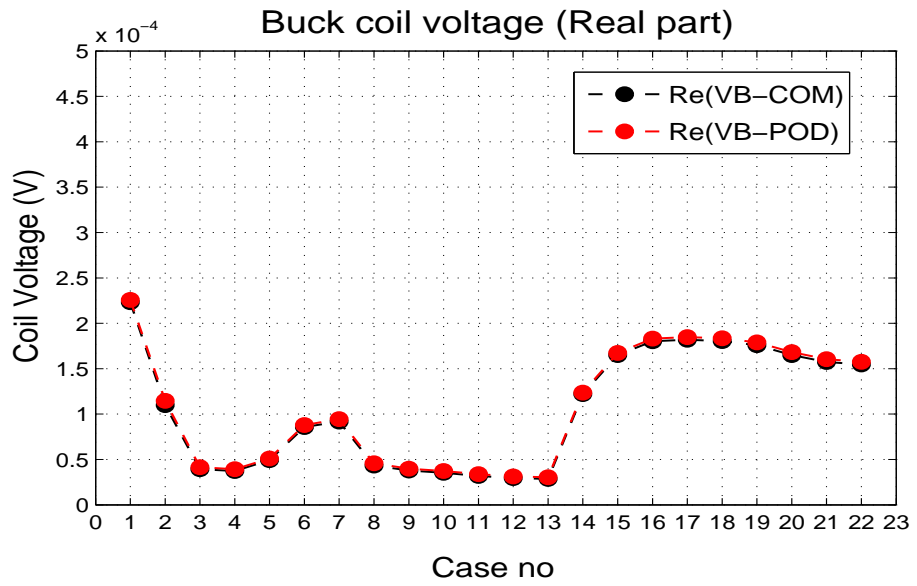
(a)
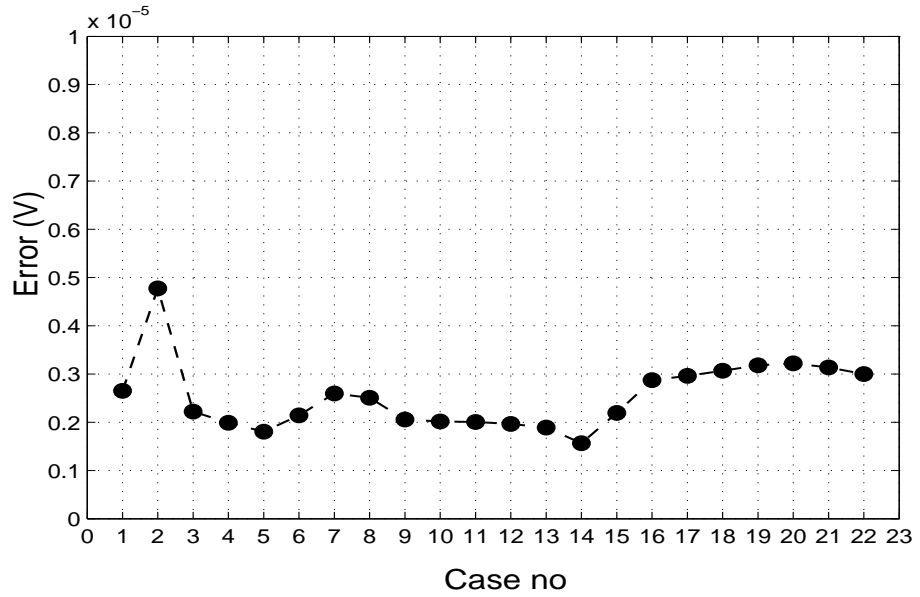
(b)

Figure 15: a) Comparison between the real part of the voltages of Bucking coil calculated from COMSOL and POD solutions for unseen cases (Table 2). b) the absolute error between the calculated voltages from POD and COMSOL solution.
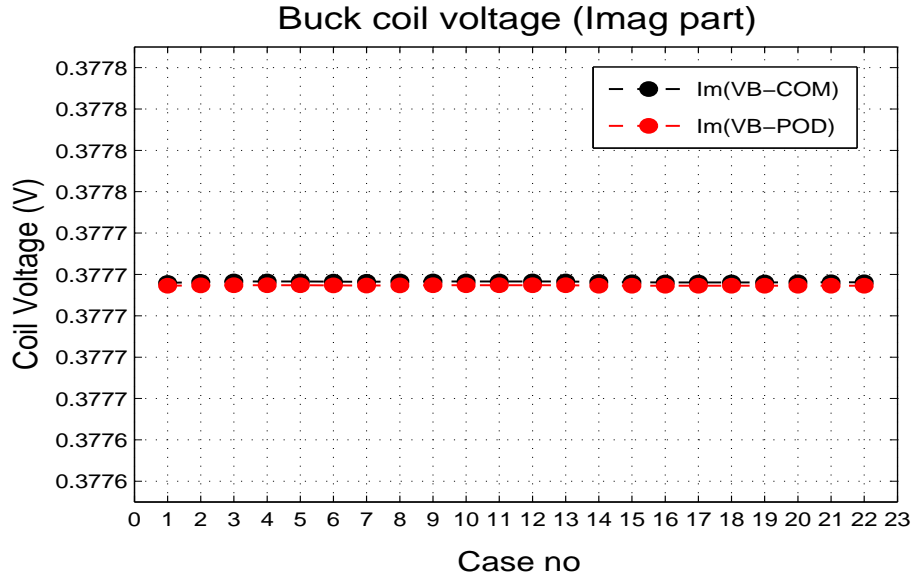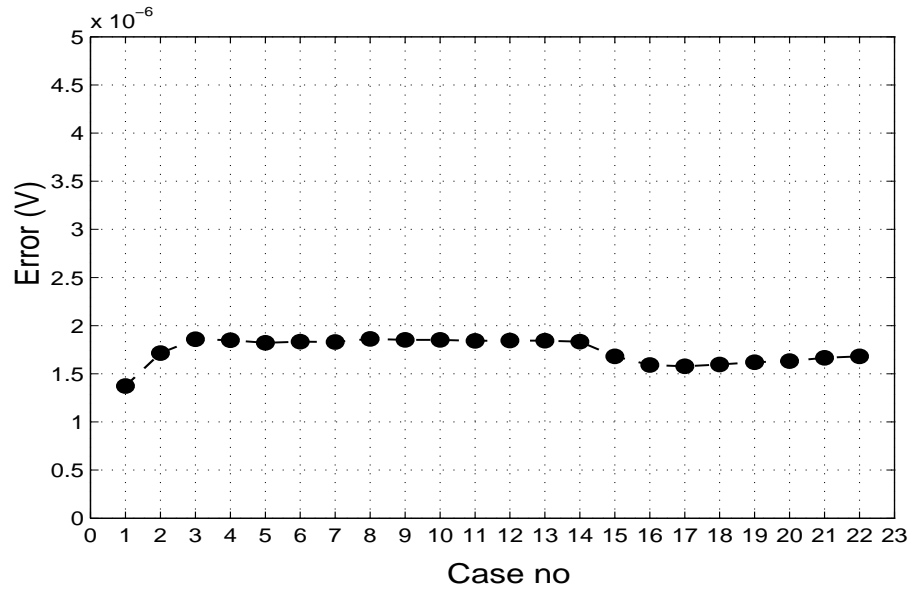
Figure 16: a) Comparison between the imaginary part of the voltages of Bucking coil calculated from COMSOL and POD solutions for unseen cases (Table 2). b) the absolute error between the calculated voltages from POD and COMSOL solution.